LANGMUIR Article
Cite This: Langmuir 2019, 35, 4946−4955
pubs.acs.org/Langmuir

Convectively Assembled Monolayers of Colloidal Cubes: Evidence of Optimal Packings

Janne-Mieke Meijer,*[,†,‡,∥] Vera Meester,[†,⊥] Fabian Hagemans,[†,#] H.N.W. Lekkerkerker,[†] Albert P. Philipse,[†] and Andrei V. Petukhov[†,§]

[†]Van 't Hoff Laboratory for Physical and Colloid Chemistry, Debye Institute for Nanomaterials Science, Utrecht University, Padualaan 8, 3584 CH Utrecht, The Netherlands

[‡]Department of Physics, University of Konstanz, Universitätstrasse 10, D-78457 Konstanz, Germany

[§]Laboratory of Physical Chemistry, Department of Chemical Engineering and Chemistry, Eindhoven University of Technology, P.O. Box 513, 5600 MB Eindhoven, The Netherlands

ABSTRACT: We employ a system of cubic colloids with rounded corners to study the close-packed monolayers that form via convective assembly. We show that by controlled solvent evaporation large densely packed monolayers of colloidal cubes are obtained. Using scanning electron microscopy and particle-tracking algorithms, we investigate the local order in detail and show that the obtained monolayers possess their predicted close-packed optimal packings, the Λ_0-lattice and the Λ_1-lattice, as well as the simple square-lattice and disordered packings. We further show that shape details of the cube corners are important for the final packing symmetry, where the frequency of the Λ_1-lattice increases with decreasing roundness of the corners, whereas the frequency of the Λ_0-lattice is unaffected. The formation of both optimal packings is found to be a consequence of the out-of-equilibrium formation process, which leads to small shifts in rows of cubes, thereby transforming the Λ_1-lattice into the Λ_0-lattice.

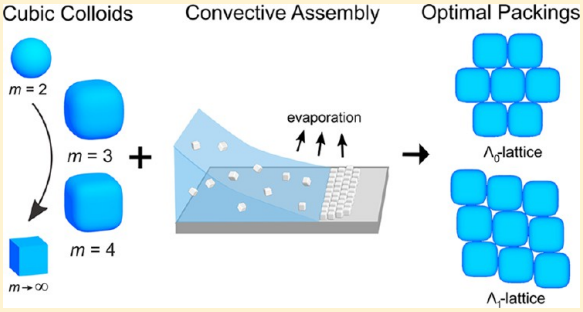

INTRODUCTION

The self-assembly of colloids into ordered arrangements is of interest for a wide range of applications, such as photonics,[1,2] chemical sensing,[3] biomimicry,[4,5] and solar cells.[6] Over the past years, several self-assembly approaches have flourished with specific features in terms of complexity of the implementation, sensitivity to process parameters, and characteristics of the final colloidal assembly; for extensive reviews, see refs 7 and 8. Convective assembly (CA) is one of the convenient preparation methods of colloidal films with a controllable thickness on a substrate.[1,7−10] The assembly of the colloidal particles occurs at the contact line between the colloidal sol and the substrate. Here, the colloids on the substrate protrude through the liquid−air interface, which induces strong immersion capillary attractions between the colloids that dominate the densification process.[11−13] Subsequently, a convective flow is induced by the solvent evaporation from the meniscus that brings additional colloids to assembling structures.[13,14]

Particle shape is well known to influence the crystal symmetry of close-packed structures formed by colloids.[15,16] Thanks to breakthroughs in colloid synthesis, many types of micron-sized colloids with well-defined anisotropic shapes and interactions have recently become available.[17−21] These colloids can be almost as complex as their atomic and molecular counterparts and provide the possibility to form a rich variety of superstructures.[20−23] It is of fundamental and practical interest to study close-packed structures of these nonspherical colloids, and the CA technique would be very suitable for their controlled assembly. So far, CA has been applied to several nonspherical shapes, including rods, ellipsoids, and bowls,[24−26] but many more shapes still need to be explored.

Recently, an anisotropic colloidal system of monodisperse hollow silica cubes was developed.[27−31] These colloidal cubes possess slightly rounded corners and can be described by a superball shape, given by[32]

$$\left|\frac{x}{a}\right|^m + \left|\frac{y}{a}\right|^m + \left|\frac{z}{a}\right|^m \leq 1 \qquad (1)$$

where m is the shape parameter, which indicates the extent of deformation from a sphere ($m = 2$) to a cube ($m \to \infty$), and a is half the edge length L. In a previous study, we have shown that these hollow silica cubes can also be assembled into large monolayer and multilayer crystalline structures via a CA method in which the substrate is placed vertically, i.e., vertical deposition (VD).[28] Interestingly, molecular dynamics and Monte Carlo simulations predict that the crystal order of the cubes can be tuned by the shape parameter m.[33,34] Especially in

Received: December 31, 2018
Revised: March 11, 2019
Published: March 15, 2019

DOI: 10.1021/acs.langmuir.8b04330
Langmuir 2019, 35, 4946−4955

the range of m accessible with these hollow cubes, $m \approx 2.5-4$, the cube shape changes from a very rounded cube to a slightly rounded cube, and a symmetry switch for both two-dimensional (2D) and three-dimensional (3D) crystal structures was found. Experimentally, the sensitivity of the equilibrium self-assembly of the hollow cubes to m has been confirmed.[30,31] For depletion-induced assembly of the cubes in quasi-2D, the formation of hexagonal, rhombic, and simple cubic-lattices was revealed, which depended strongly on m and the size ratio between the cube and the depletant.[30] In addition, the sedimentary 3D crystals formed by the cubes were found to form plastic face-centered cubic crystals that upon an increase in concentration transitioned into predicted hollow-site rhombic crystals for $m \leq 3.4$, whereas for $m \geq 3.4$, an unpredicted bridge-site rhombic crystal structure was found.[31]

The main aim of this study is to address the effect of the colloidal cube shape details on the structure of densely packed monolayers assembled via CA, which is an out-of-equilibrium process. We employ three colloidal cubes with different m-values and use different CA methods to assemble the colloidal cubes. We investigate the formed monolayer structures in detail with scanning electron microscopy (SEM). We developed image analysis routines to detect the local packing arrangements and quantify the occurrence of different lattices packings. We find that several different packings occur as a consequence of the cubic shape and the out-of-equilibrium formation process.

EXPERIMENTAL SECTION

Colloidal Cube Synthesis. For the synthesis of three different types of hollow silica cubes, we first synthesized three different template hematite particles with a cubic shape following the sol–gel procedure.[27,31,35] Briefly, to obtain hematite cubes with an edge length L = 932 nm, 50.53 g of $FeCl_3 \cdot 6H_2O$ (Sigma-Aldrich, 99%) was dissolved in 100.0 mL of water, followed by rapid mixing (20 s) with 20.18 g of NaOH dissolved in 100.0 mL of water under vigorous magnetic stirring. Next, the suspension was aged at 100 °C for 8 d during which the hematite cubes were formed. The hematite cubes were cleaned by repeated centrifugation and redispersion in water. Water from a Millipore system was always used.

The hollow silica cubes were prepared by coating the hematite cubes with amorphous silica using an adaption of the Stöber synthesis.[27,36] First, the hematite cubes were functionalized with polyvinylpyrrolidone (PVP). This was done by mixing 50.0 mL of 7 wt % hematite cubes in water with 10.0 g of PVP (M_w 40 000 g/mol, Aldrich) in 100.0 mL of water and stirring overnight. Next, the functionalized cubes were washed by repeated centrifugation and redispersion in ethanol (96%, Interchem) to a final concentration of 4.7 wt %. Next, 75.0 mL of PVP-functionalized hematite cubes in ethanol was mixed with 800 mL of ethanol, 15.0 mL of 1.0 wt % tetramethylammonium hydroxide (Fluka) solution, and 122.0 mL of water. To this mixture, 20.0 mL of TEOS (98%, Sigma-Aldrich) mixed with 20.0 mL of ethanol (p.a., Aldrich) was added dropwise over the course of ~3 h under mechanical stirring and sonication. Next, the silica-coated hematite cubes were cleaned by washing via repeated centrifugation and redispersion in water. The hematite core was removed by dispersing the cubes in ~5 M HCl (Merck) over a period of 24 h. The core is removed because hematite has a permanent dipole moment and influences their self-assembly in 2D.[37] This step is followed by repeated washing, and finally, the hollow cubes were stored in ethanol to prevent silica etching, which may occur in water.

All colloids were characterized with transmission electron microscopy (TEM, Philips TECNAI 10 or 12). Figure 1a,b shows typical TEM images of a template hematite cube and the hollow silica cube obtained from this. The average edge length $\langle L \rangle$, the polydispersity σ_L, the average silica shell thickness $\langle t_{SiO_2} \rangle$, and the shape parameter m of the cubes were determined by analyzing more than 100 TEM images. The specific properties of all hematite and hollow silica cubes are shown in Table 1. The hollow silica cubes in this study were found to have the shape parameter m ranging from 2.9 to 3.6, allowing us to study the effect of a specific shape on the convective assembled structures in an m range where switching crystal symmetries are predicted.[32−34]

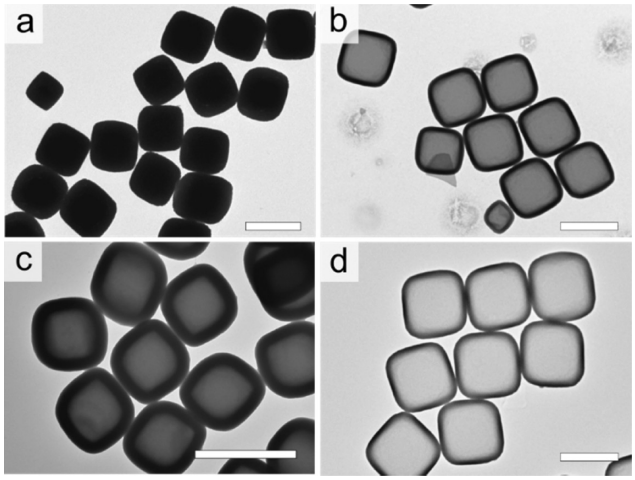

Figure 1. TEM images of (a) hematite cubes II and (b–d) hollow silica cubes with different m-values: (b) II_Si with m = 3.5, (c) I_Si with m = 2.9, and (d) III_Si with m = 3.6; see Table 1 for details. Scale bars are 1 μm.

Table 1. Characteristics of the Hematite and Hollow Silica Cubes

	$\langle L \rangle$ (nm)	σ_L (nm)	$\langle t_{SiO_2} \rangle$ (nm)	m
Hematite				
I	558	6		3.7
II	932	6		[a]
III	1180	4		[a]
Hollow				
I_Si	774	35	108	2.9
II_Si	1033	45	50	3.5
III_Si	1266	27	43	3.6

[a] m not determined.

Sample Preparation. Prior to convective assembly experiments, a 5.0 vol % stock dispersion of hollow silica cubes in water was prepared by repeated centrifugation. The cubes consist of thin hollow silica shells whose volume is hard to estimate, which obstructs the determination of the volume fraction from the weight concentration of the stock suspensions. Therefore, the stock suspensions were centrifuged at 680g in thin 100 × 4 × 0.2 mm^3 capillaries. Assuming that the sediment has a random packing density of 72–80 vol % based on their shape,[38] the volume fraction was estimated from the obtained sediment volume. The desired volume fractions were achieved by diluting the stock dispersions with the appropriate amount of water. Cube dispersions in water with a volume fraction in the range of 0.1–0.5 vol % were used as these were empirically found to result in large monolayer deposits.

Microscope glass slides with dimensions of 24 × 50 mm^2 (Menzel-Gläzer #1.5) were cut to 12 × 50 mm^2 using a diamond pen followed by etching with 7.0 wt % KOH (Merck) in 7.0 wt % aqueous solution in ethanol for at least 1 h but usually 16 h. Subsequently, the slides were rinsed thoroughly with ethanol and water, followed by drying in air before use.

DOI: 10.1021/acs.langmuir.8b04330
Langmuir 2019, 35, 4946–4955

Convective Assembly. Due to the size difference between the cubes (see Table 1), two different convective assembly methods were employed to induce the formation of dense cube packings. For the smallest cubes, we employed the vertical deposition (VD) method, as described in our earlier work[28] and schematically shown in Figure 2a.

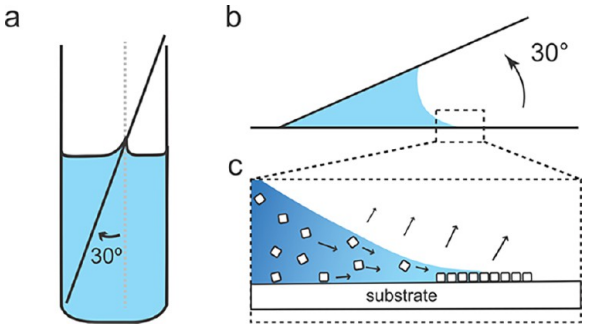

Figure 2. Schematic representations of (a) vertical deposition (VD) method where a substrate is immersed vertically in a colloidal dispersion. (b) Horizontal deposition (HD) method where a substrate is placed horizontally and the second one is positioned at an angle of 30°, and (c) convective particle assembly close to the air−solvent−substrate contact line due to solvent evaporation and immersion capillary forces.

For the larger cubes, we used a horizontal deposition (HD) method.[39] The HD method is used because the larger size leads to a higher sedimentation velocity and reduces the cube concentration close to the contact-line too fast for the use of the VD method. The main difference is the orientation of the microscope slide onto which the dense structure of cubes forms. A schematic illustration of the HD method is shown in Figure 2b. Two microscope slides are placed in a wedge shape, with one horizontal and the second slide placed with an angle of 30° on top of the first. A droplet placed into the corner formed by the two slides will cause the meniscus to have a concave shape. In both methods, cubes will be pinned in the thin layer of the solvent on the substrate, and due to the convective flow, more cubes will be transported to this region, causing the formation of dense packings, as schematically shown in Figure 2c.

For the VD experiments, a small wide-neck vial was filled with 2.5 mL of cube dispersion and a clean substrate was placed into the colloidal sol at an angle of 30°. Next, the vial was placed in an oven at 50−70 °C for at least 24 h to allow the solvent to evaporate. For an HD experiment, 100.0 μL of dispersion was placed in the corner of the slides and the slides were covered with a 2*L* crystallization dish to avoid irregular air flow. Slow solvent evaporation occurred over 8 h at room temperature. During solvent evaporation, cube deposits form on the substrate. By controlling the cube concentration, dominant monolayer structures can be obtained. However, due to an increase in concentration upon solvent evaporation, eventually multilayer structures will also form, but these are out of the scope of the current investigation.

The convectively assembled deposits were imaged with SEM using a Phenom FEI microscope. High-resolution SEM images were obtained using an FEI XL30S FEG. The samples were connected with carbon tape to an SEM specimen stub and coated with a 6−8 nm layer of platinum using a sputter coater.

Image Analysis. The particle center of mass and angle of the longest diagonal, α, with respect to the *x*-axis of the images were retrieved from the SEM images using analysis iTEM software. For this, a threshold was determined and the image was binarized. A series of erosion steps were performed until all particles could be identified by eye. The centers were used for a Voronoi construction that was subsequently overlaid on the first binarized image. In this way, the cubes were clearly separated while maintaining their shape. Next, using particle detection algorithms, the center of mass and orientation of the longest diagonal of each cube were determined. Further analysis of the nearest neighbor (NN) positions and lattice identification were performed with specialized analysis routines written in IDL (Interactive Data Language, Harris Geospatial Solution, Boulder, Colorado).

RESULTS AND DISCUSSION

Monolayer Structure and Order. With the convective assembly methods, extended monolayer films were obtained for all three types of cubic colloids. The crystallinity of these films manifested itself by the presence of strong Bragg reflections of the visible light. The monolayers were investigated in detail with SEM. Figure 3 shows typical SEM images for all three differently shaped and sized colloidal cubes. Here, very densely packed structures can be observed in which the cubes have all oriented flat on the substrate. Some cracks and additional spacing can be observed between the cubes, which are typical for convective assembled structures and are caused by drying effects and the exposure to the electron beam. The densely packed structures and orientation of the cubes can be explained by their shape and the convective assembly process. During the evaporation of the solvent from the dispersion, cubes close to the air−water−substrate contact line become pinned between the meniscus of the thin solvent layer and the substrate, which forces them into a flat orientation. In addition, the distortion of the solvent−air interface induces strong immersion capillary forces between the cubes,[11] resulting in the formation of dense packings. The cubes in turn pin the contact line, and due to the evaporation of the solvent from the thin solvent film, a strong flow toward the contact line is induced. This flow transports cubes to the already formed close-packed structure causing the structure to grow.

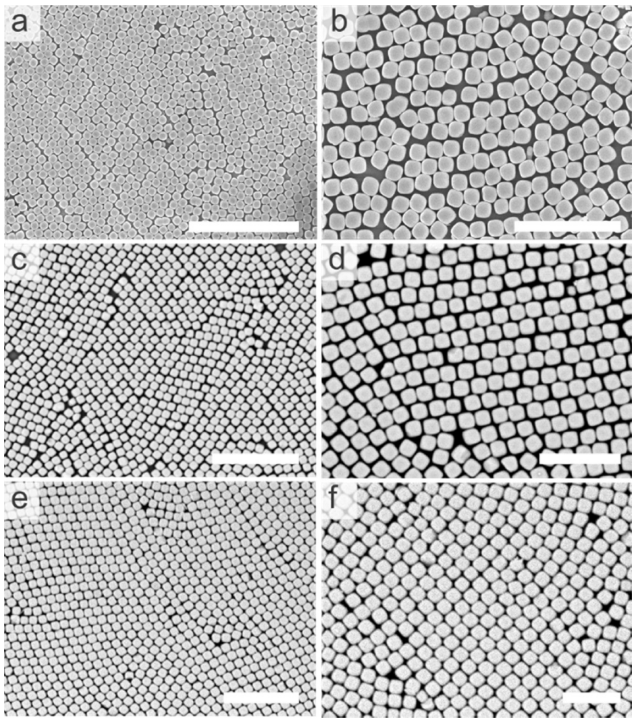

Figure 3. Typical SEM images of the obtained monolayers of the hollow silica cubes with different *m*-values. (a, b) m = 2.9, (c, d) m = 3.5, and (e, f) m = 3.6. Scale bars are (a, c, e) 10 μm and (b, c, f) 5 μm.

DOI: 10.1021/acs.langmuir.8b04330
Langmuir 2019, 35, 4946−4955

In the densely packed monolayers, domains with different positional and orientational orders can be observed. Closer investigation of the structures revealed that several different types of dense packings can be identified, ranging from optimal to disordered packings. Figure 4a,b shows the Λ_0-lattice and

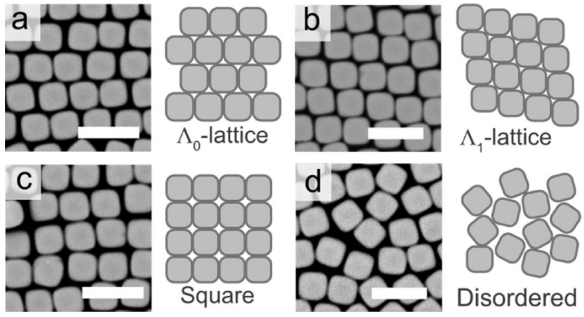

Figure 4. SEM images of the different types of dense packings observed for cubes with m = 3.5. (a) Λ_0-lattice, (b) Λ_1-lattice, (c) simple square-lattice, and (d) disordered packings. Scale bars are 2 μm.

the Λ_1-lattice, which are the densest packings found with molecular dynamic simulations for a superdisk, which is the 2D equivalent of a superball.[33] The formation of these two superdisk packings is caused by the fact that in the monolayer the cubes interact only via their sides and thus essentially only via their 2D "superdisk" shape. In addition, a simple square-lattice packing (Figure 4c) and rotationally disordered packings (Figure 4d) were observed. The observation of these latter two packings is surprising as these have a lower packing density, whereas the immersion capillary forces between the cubes are quite high. The formation of these packings might therefore be caused by a too strong pinning of the cubes between the meniscus and substrate during the solvent evaporation.

Lattice Criteria. To investigate the local packings in more detail, we need to correlate the positional and orientational orders in the different lattices. Therefore, we first defined the criteria to assign the Λ_0, Λ_1, and simple square-lattices based on the cube body orientation, α, (Figure 5a) and the NN positions with respect to α, expressed by the angle, θ (Figure 5b). The lattice vectors of the Λ_0-lattice are given by[33]

$$\mathbf{e}_1 = L\mathbf{i} \tag{2}$$

$$\mathbf{e}_2 = (L/2)\mathbf{i} + (L/2)(2^m - 1)^{1/m}\mathbf{j} \tag{3}$$

On the other hand, the lattice vectors of the Λ_1-lattice are given by

$$\mathbf{e}_1 = (L/2)2^{(1-1/m)}\mathbf{i} + (L/2)2^{(1-1/m)}\mathbf{j} \tag{4}$$

$$\mathbf{e}_2 = (L/2)(2^{-1/m} - 2^{1/2}s)\mathbf{i} + (L/2)(2^{-1/m} + 2^{1/2}s)\mathbf{j} \tag{5}$$

In both cases, $\mathbf{i}$ and $\mathbf{j}$ are the unit vectors along the x and y directions along the particle symmetry directions, L is the particle edge length, m is the deformation parameter, and s is the smallest positive root of the following equation

$$|2^{-(1+1/m)} - 2^{-1/2}s|^m + |2^{-(1+1/m)} + 2^{-1/2}s|^m = 1 \tag{6}$$

The lattice vectors for a square-lattice are given by

$$\mathbf{e}_1 = L\mathbf{i} \tag{7}$$

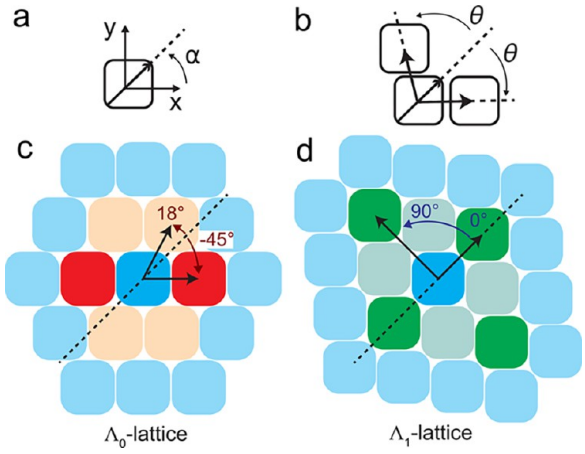

Figure 5. Schematic illustration showing how the orientations of the cubes are determined from the SEM images. (a) Angle, α, the long diagonal makes with the x-axis, (b) angle, θ, the nearest neighbors make with respect to α. Schematic illustrations of (c) Λ_0-lattice and (d) Λ_1-lattice.

$$\mathbf{e}_2 = L\mathbf{j} \tag{8}$$

Figure 5c,d shows the schematic illustration of the Λ_0 and Λ_1-lattice packings. In the Λ_0-lattice, the cubes are located in rows aligned with their faces and offset by $1/2L$, whereas in the Λ_1-lattice, the rounded corners of the cubes are touching, leading to a rhombic lattice symmetry. The packings are actually very similar from a particles' center point of view; both dark-blue center cubes have six NNs. However, the NN positions are clearly different with respect to the center cube body orientation, α, with two NNs located at the cube face for the Λ_0-lattice, whereas for the Λ_1-lattice, two NNs are located at the cube corners. For the case of a cube with m = 3.5, this leads to the following criteria. The Λ_0-lattice possesses two NNs located at distance 1.0L at an angle $\theta = \pm 45°$ (red particles, Figure 5c) and four NNs at distance 1.1L with $\theta = \pm 18°$ (orange particles, Figure 5c). The Λ_1-lattice possesses two NNs at 1.16L with $\theta = 0°$ (dark green particles, Figure 5d) and four NNs at 1.01L with $\theta = \pm 35$ or $\pm 55°$ (light green particles, Figure 5d). In addition, the Λ_1-lattice possesses two neighbors located slightly further away at 1.66L with $\theta = 90°$ (dark green particles, Figure 5d). The simple square-lattice also possesses four NNs at $\sqrt{2}L$ with θ = 0 or 90° but in addition has four NNs at L with $\theta = \pm 45°$.

The unique positions and orientations of a cube in the Λ_0-lattice, Λ_1-lattice, and square-lattice were used for the lattice identification using an analysis routine consisting of several steps. First, the position, r, and angle of the longest diagonal with the x-axis, α, of the cubes were extracted from the SEM images. For further analysis, we take into account that a cube is 4-fold degenerate and determine the body orientation, ξ_4, according to

$$\xi_4 = e^{i4\alpha} \tag{9}$$

Figure 6a shows for two differently ordered monolayers of the cubes with m = 3.5 the identification of the detected positions and orientations as indicated by the overlaid squares, which are colored according to their local ξ_4 in the complex plane.

In the second step, we identified the eight closest neighbors (also referred to as NNs for convenience) of each particle based on the relative distance to the particle center. We require eight NNs for the assignment of the Λ_1-lattice and the simple

DOI: 10.1021/acs.langmuir.8b04330
Langmuir 2019, 35, 4946−4955

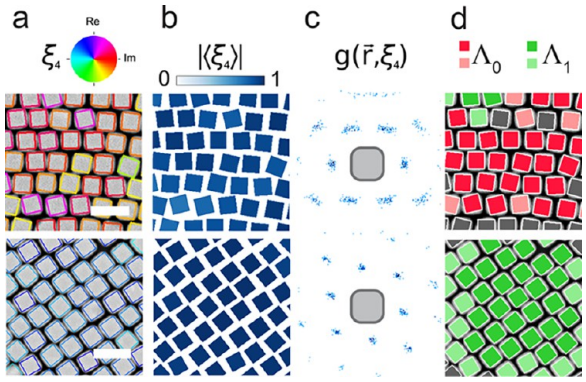

Figure 6. (a) SEM images of two regions with different lattice packings. The detected positions and orientation are represented by the squares and colored according to their body orientation ξ_4. (b) Local orientational order parameter $|\langle\xi_4\rangle|$ showing high orientational order of the nearest neighbors (NNs). (c) Bond−body correlation function $g(r, \langle\xi_4\rangle)$ of the eight closest NN positions with respect to the center cube orientation, showing a clear difference of NN positions in the two lattices. (d) Assignment of lattice type based on NN position criteria overlaid on the SEM image. Scale bars are 2 μm.

square-lattice, which cannot be obtained via the triangulation algorithm. By selecting the eight NNs on the relative distance, we also allow for fluctuations in the cube positions that occur due to cube polydispersity and drying effects. In the third step, the correlation between the NN body orientations is checked, as in the densely packed crystal lattices, the surrounding cubes should possess orientational order. For this, we take into account the alignment of the NNs by determining the local body orientational order parameter, $\langle\xi_4\rangle$, according to

$$\langle\xi_4\rangle = \frac{1}{N}\sum_{j}^{N}\xi_{4,j} \tag{10}$$

where N is the total number of NNs. If the NNs possess high orientational order, $|\langle\xi_4\rangle| \sim 1$, whereas the absence of orientational order between the NNs leads to $|\langle\xi_4\rangle| \sim 0$. Figure 6b shows the local $|\langle\xi_4\rangle|$ value for each cube in the different structures, showing that in these two cases the local order is high. We employed a minimum value of $|\langle\xi_4\rangle| = 0.6$ to identify the particles with high degree of body orientational order because this was empirically found to identify the ordered particles well while taking into account the small detection error in α.

Next, in the fourth step, we determined θ for the NNs. To reduce the observed error in α detection, we employ the average $\langle\xi_4\rangle$ based on the assumption that in the lattices the cubes have the same orientation (although we use the center ξ_4 when the angle difference between $\langle\xi_4\rangle$ and ξ_4 was found to be larger than 0°). Figure 6c shows the bond−body correlation function $g(r, \xi_4)$, which visualizes the local density plot of the neighbor positions with respect to the cube body orientation, ξ_4. Here, the difference in NN positions in both lattices can be clearly seen. Finally, in the fifth step, the local lattice packing is assigned based on the number of NNs with specific θ according to selection criteria. We distinguish between the Λ_1-lattice and the square-lattice, which both have four NNs located at 0 or 90°, by determining the bond length ratio, b_L, of the two shortest with the two longest bonds. For the simple square-lattice, $b_L \approx 1.0$, whereas for the Λ_1-lattice, $b_L \approx 1.4$, and we use a cutoff value of $b_L = 1.2$. The "perfect" lattices are those that meet the full lattice criteria, whereas the "defect" lattices are assigned to those particles for which one of the perfect criteria is not fully met. In Table 2, the exact criteria for the lattice assignment are given. We allow for small deviations from the ideal lattice positions due to drying effects and detection errors by allowing a deviation in θ of $\sigma = 10\%$. In case none of the criteria are met, the particle is labeled as not assigned.

Table 2. Selection Criteria for the Assignment of Each Lattice, Based on the Number of NNs with Specific θ

	θ			
	±45° σ = 5°	±18° σ = 10°	0°/±90° σ = 10°	b_L
Λ_0	2	4		
Λ_0-defect	2	3	≤2	
	1	4	≤2	
Λ_1			4	≥1.2
Λ_1-defect	≤1		3	
Sq	≥3		4	<1.2
Sq-defect	≥2		4	<1.2
	≥3		3	

Lattice Identification. With the established analysis routines, all monolayers were analyzed. Figure 7 shows three typical SEM images of monolayers formed by the cubes with m = 3.5 and the different analysis results. In these images, all three lattices, as well as some defects, can be observed. Figure 7a shows a large monolayer region that clearly possesses a high degree of orientational order (Figure 7d) and is overall identified as the Λ_1-lattice (Figure 7g). Besides highly ordered monolayers, also monolayers with a gradual rotation of the cube body orientation were observed, as shown in Figure 7b. The change in body orientation does not destroy the local alignment of cubes (Figure 7e). The orientational change, however, is related to a continuous transformation of the Λ_1-lattice to the Λ_0-lattice in the form of switching rows of cubes. In addition, between the rows, also some square-lattice packings can be observed (Figure 7h). Figure 7c shows a monolayer in which many small particles and doublets (particle grown together during the silica-coating process), as well as stacking faults, can be observed, as indicated by the arrows in Figure 7c. The orientational analysis (Figure 7e) shows that a large degree of orientational disorder is present on the right side of the image. In addition, the ordered regions on the left side were found to have formed a hexagonal or square symmetry (red dashed boxes). The lattice analysis (Figure 7f) reveals that there are two large regions of both the Λ_0-lattice and Λ_1-lattice and some regions with the square-lattice, whereas the disordered region has not been assigned. The low number of particles identified as having a square-lattice, even though by eye, several regions could be identified (Figure 7f), seems to be a consequence of the low persistence of the structure. A shift of two rows of cubes leads to a local square arrangement, but for assignment, three rows have to align, which does not occur often. Evidently, monolayers of cubes, assembled via the convective assembly method, form ordered and disordered packings. In the ordered packings, the formation of the two densest packings, the Λ_0-lattice and Λ_1-lattice, occurs with a higher tendency to form the Λ_1-lattice, and only on very few occasions, the less densely packed simple square-lattice is formed.

DOI: 10.1021/acs.langmuir.8b04330
Langmuir 2019, 35, 4946−4955

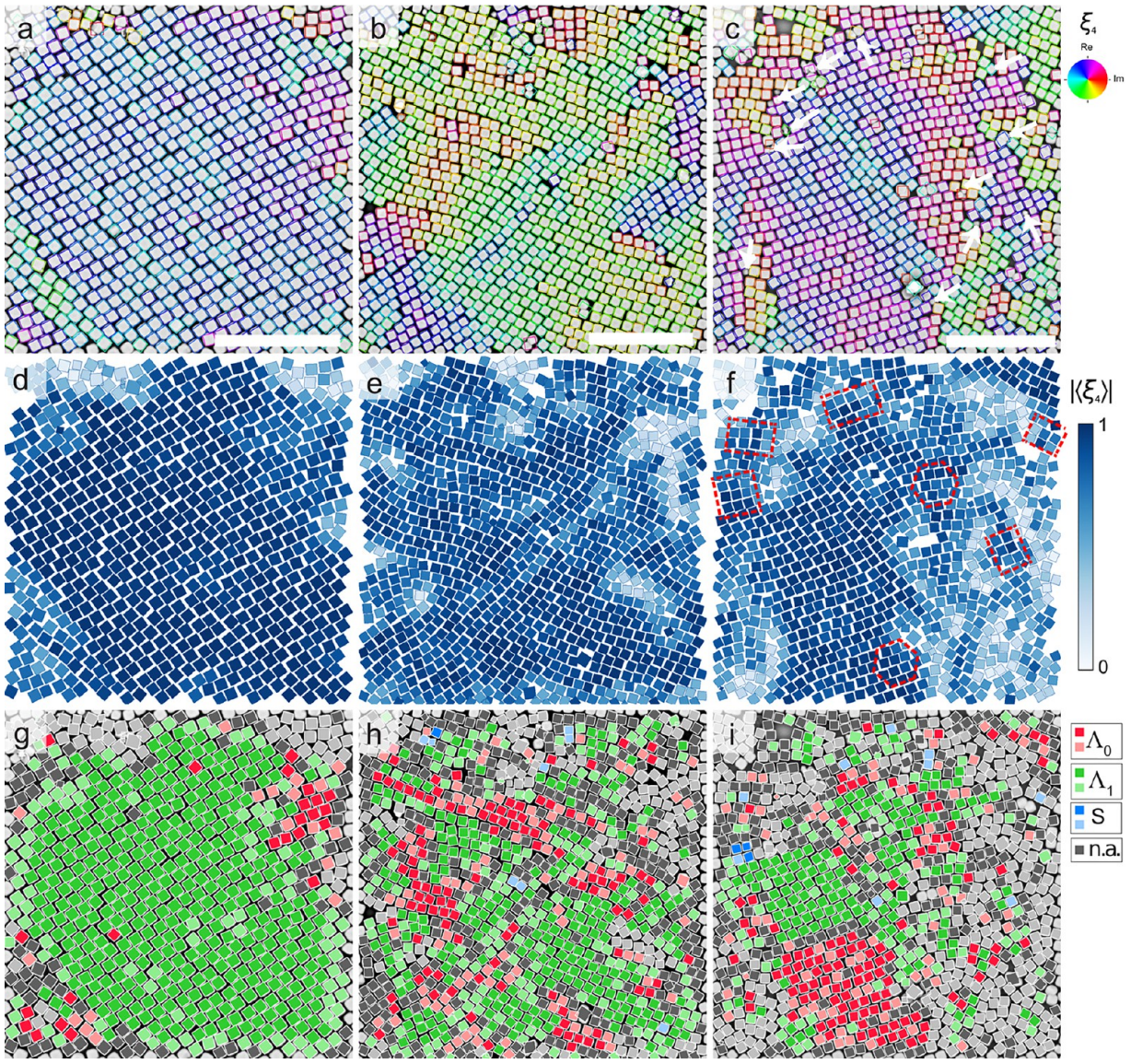

Figure 7. (a–c) SEM images of monolayers of cubes with m = 3.5. The particle coordinate and orientation are indicated by the overlaid squares colored according to their body orientation, ξ_4, in the complex plane. (d–f) Local orientational order parameter $|\langle\xi_4\rangle|$ for each particle, showing clear regions with high and low order. (g–i) Assignment of the local lattice for particles. The Λ_0-lattice (red), Λ_1-lattice (green), square-lattice (blue), with local $|\langle\xi_4\rangle| > 0.6$ but not assigned (dark gray), and with local $|\langle\xi_4\rangle| < 0.6$ (light gray) are indicated. Scale bars are 10 μm.

Influence of Shape. The effect of shape was further analyzed by investigating the monolayers formed by the cubes with m = 2.9 and 3.6. Figure 8 shows two typical images of the lattice analysis for both cubes. For the cubes with m = 2.9, we find that both the Λ_0-lattice and Λ_1-lattice coexist with relatively short-range ordered regions (Figure 8a,b). Also, it is clear that a large degree of orientational disorder is present as many cubes were not analyzed (light gray cubes) due to low local orientational order $|\langle\xi_4\rangle| < 0.6$, but also many of the local ordered cubes (dark gray) have not been assigned a lattice. One reason for this high disorder is that these rounded cubes can rotate easily in their dense packings, as, for instance, observed in the center of Figure 8a, where a 90° rotation of the cubes occurs on a row, but the overall lattice is not disturbed. For the less-rounded cubes with m = 3.6, the analysis shows that large regions with the Λ_1-lattice are present, which are intersected with single particles, rows, and/or short-ranged regions of the Λ_0-lattice (Figure 8c,d). Also, most of the particles have been assigned a lattice, indicating high local orientational order.

We note that in this study the larger m also encompasses an increase in L, as the cubes with m = 3.6 are almost twice the size of the cubes with m = 2.9. A larger size will lead to slightly stronger immersion capillary forces[11] that might contribute to the increase in orientational order and hence the formation of the Λ_1-lattice. However, many simulation studies[22,32−34,40] as well as studies on nanocubes[41] show that the exact shape of the cubes is the main factor that controls the packing of crystalline structures. Especially, a previous study of our lab[30] employing similar sized hollow cubes assembling via depletion interaction showed that a change in m from 3.0 to 3.9 also induces a change from the Λ_0 to the Λ_1-lattice in 2D structures. Therefore, we conclude that the higher orientational order and more dominant Λ_1-lattice formation are mainly caused by the higher m-value of the cubes and not their size.

DOI: 10.1021/acs.langmuir.8b04330
Langmuir 2019, 35, 4946−4955

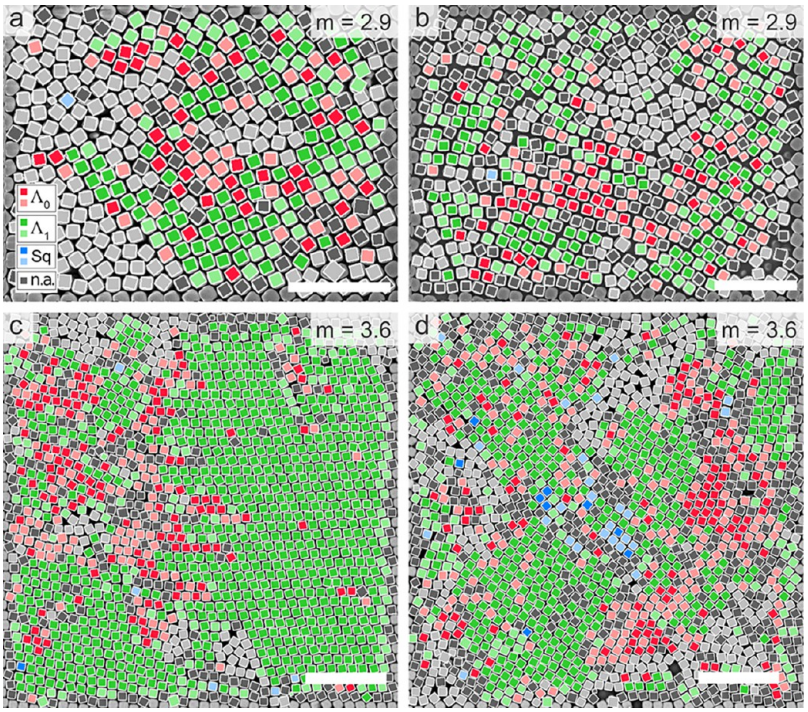

Figure 8. Lattice analysis result for cubes with (a, b) m = 2.9 and (c, d) m = 3.6. The Λ_0-lattice (red), Λ_1-lattice (green), square-lattice (blue), with local $|\langle\xi_4\rangle| > 0.6$ but not assigned (dark gray), and with local $|\langle\xi_4\rangle| < 0.6$ (light gray) are indicated. Scale bars are (a, b) 5 μm and (c, d) 10 μm.

To quantify the overall difference in lattice packings, we determined the overall orientational order and the frequency of each lattice assignment in all monolayers of the different cubes. Figure 9a shows for each cube the percentage of particles with $|\langle\xi_4\rangle| > 0.6$ found in each of the analyzed monolayers. This clearly shows that a larger m-value of the cubes causes the formed structures to be more orientationally ordered. Figure 9b shows the histograms of the lattice assignment including the percentage of cubes that could not be assigned a specific lattice type. From the histogram, it is clear that for each cube the Λ_1-lattice is the most dominant packing and the dominance increases with m. In addition, a common trend is observed for the cubes as the Λ_0-lattice occurs with the same frequency of ~20%, as well as the square-lattice with ~2−3%. This trend indicates that the formation of both the Λ_0-lattice and the square-lattice is controlled by another parameter than m and seems to be related to the convective assembly process, as discussed later. Evidently, the Λ_1-lattice increase occurs only at the expense of the disordered particles. For the cubes with m = 3.6, we even find that 40% of all particles possess a local Λ_1-lattice packing. This effect is so strong that in the radial distribution function, $g(r/L)$, the dominance of the Λ_1-lattice is visible. Figure 9c shows the average $g(r/L)$ obtained from the monolayers of each cube. It is clear that for m = 2.9 the orientational disorder and presence of both lattices lead to distinct peaks at L but no clear lattice can be assigned, whereas for m = 3.6, distinct peaks are visible in $g(r/L)$, which can be identified as the peaks of the Λ_1-lattice. In addition, we also investigated the average domain size for the particles assigned a perfect lattice, as shown in Table 3. For each m, we found a large distribution of domain sizes, with many small domains (2−4 particles) and larger domains with widespread sizes (up to 500 particles). Even though this causes a large standard

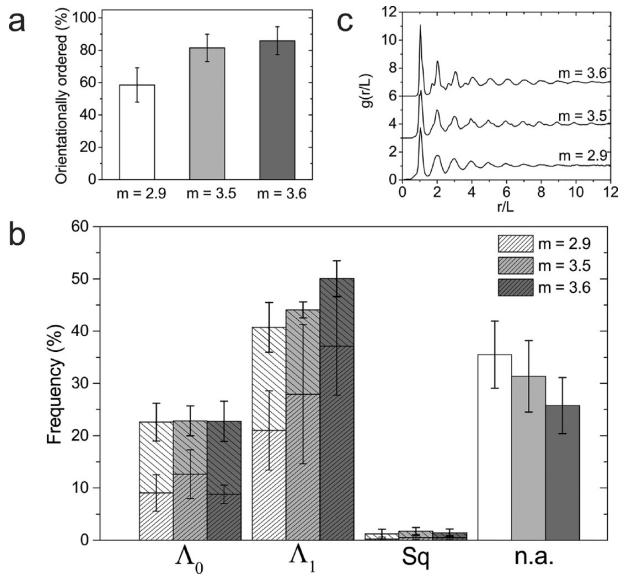

Figure 9. (a) Amount of orientationally ordered particles with $|\langle\xi_4\rangle| > 0.6$ observed in the monolayers formed by the cubes with different values for the shape parameter m. (b) Distribution of the assigned lattice to the orientationally ordered particles for each cube. For the lattices, the perfect (densely dashed) and defect (medium dashed) assigned particles are cumulated. (c) Average radial distribution $g(r/L)$ for the monolayers of each m.

Table 3. Average Domain Size for the Different Lattices

cube	Λ_0	Λ_1	Sq
m = 2.9	3.5 ± 2.1	6.3 ± 10.3	2[a]
m = 3.5	6.4 ± 9.2	9.1 ± 23.5	2.5 ± 0.7
m = 3.6	4.5 ± 4.9	17.1 ± 55.8	3.5 ± 1.8

[a]Only one cluster observed.

DOI: 10.1021/acs.langmuir.8b04330
Langmuir 2019, 35, 4946−4955

deviation in the overall average size, the same trend is observed: with increasing m, the Λ_1-lattice domains grow, whereas the Λ_0-lattice domains remain a limited size. Clearly, cubic colloidal monolayers formed via CA show the formation of the optimal packings for these rounded cubes, the Λ_0-lattice and Λ_1-lattice, as well as less dense structures with a simple square-lattice or rotationally disordered packings. Moreover, the orientational order as well as the occurrence of the Λ_1-lattice can be controlled by the shape parameter.

Our finding that hollow cubes form the optimal Λ_0-lattice and Λ_1-lattice packings is in agreement with previous investigations on the densest packings of superdisks[33] and hollow cubes assembling via depletion interaction.[30] However, the observation that both the Λ_0-lattice and Λ_1-lattice packings occur side by side in a monolayer is different from these studies and also does not agree with experiments and simulations of rounded squares,[40,41] where at high ϕ and m, only the formation of the Λ_1-lattice was observed The fact that we observe both optimal lattice packings seems to be related to the different formation mechanisms. Whereas the other studies investigated equilibrium assembly, we employed CA, which is an out-of-equilibrium assembly process. It is well known that at equilibrium the realization of the highest possible packing density will occur. For instance, precious opals or synthetic colloidal crystals consisting of spheres of two different sizes will form AB_{13} structures,[42−44] and also many anisotropic nanoparticles and colloids have been observed to form their most densely packed structures.[45,46] In contrast, CA involves strong immersion capillary forces, which lead to attractive capillary interaction energies of $\sim 10^6\ kT$ for 1 μm particles,[11] as well as fast solvent flows and convective transport of the cubes that distort the equilibrium packings. The packings can be further influenced by the small polydispersity (7%) in size and shape of the cubes, as well as pinning of the cubes to the substrate. These factors do not allow the cubes to explore all of the possible configurations during assembly, and the densely packed structures will contain nonequilibrium packings and defects.

Besides the small differences between the Λ_0-lattice and the Λ_1-lattice, their packing densities are very similar, $\phi_{\Lambda 0} = 0.933$ and $\phi_{\Lambda 1} = 0.940$ for $m = 3.5$, and although the lattices are rotationally different due to their cubic shape, the NNs are aligned in rows along the cube faces. A small shift in the position of a row combined with a minimum rotation of the cubes already transforms the Λ_1-lattice into the Λ_0-lattice and vice versa. Figure 10 shows a schematic representation of this row-shifting process. The same process can also lead to the formation of the simple square-lattice. However, due to the finite roundness of the cube faces, the square-lattice has a relative lower packing density of $\phi_S = 0.898$. Hence, this lattice will be less stable under the influence of the strong capillary forces and explains the low frequency of the packing. Small disturbances in the assembly process, such as the pinning of cubes, can easily induce such row-shifts. These disturbances are method dependent and explain why the amounts of the Λ_0-lattice and the square-lattice are the same for each cube, irrespective of the cube m-value. Therefore, we conclude that the observed lattices in the convectively assembled monolayers of cubes are a result of the combination of the cube shape and out-of-equilibrium assembly process.

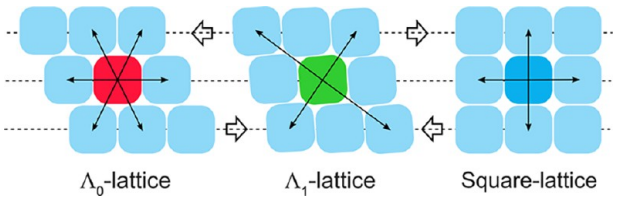

Figure 10. Schematic illustration of the transition of the Λ_1-lattice into the Λ_0-lattice or the square-lattice by a small shift of the top and bottom rows of cubes along the direction of the big arrow.

Defect Structures. To further investigate the effects of the out-of-equilibrium process, we studied the defects and other types of disorders in the monolayers. One striking observation is the almost complete absence of vacancies, which typically occurs in monolayers of spheres obtained via convective assembly or spin-coating.[47] We did observe that particles were displaced from the inside to the top of the monolayer due to the physical manipulations necessary for the SEM preparation, but these always came in pairs. This vacancy absence seems to be related to the alignment of cube faces, which allows rows of cubes to easily shift and fill up any vacancy that might have formed. Something similar has been observed in simulations of sharp-edged cubes, where vacancies delocalize.[48] Furthermore, clear grain boundaries between different ordered domains were not often observed. Instead, we observed several different types of orientational disorder. Figure 11a shows, for cubes with $m = 2.9$, how the very rounded cubic shape allows rotations of the cubes. For the local particle centers, we determined the local 6-fold bond-orientation order parameter Ψ_6, which is defined as

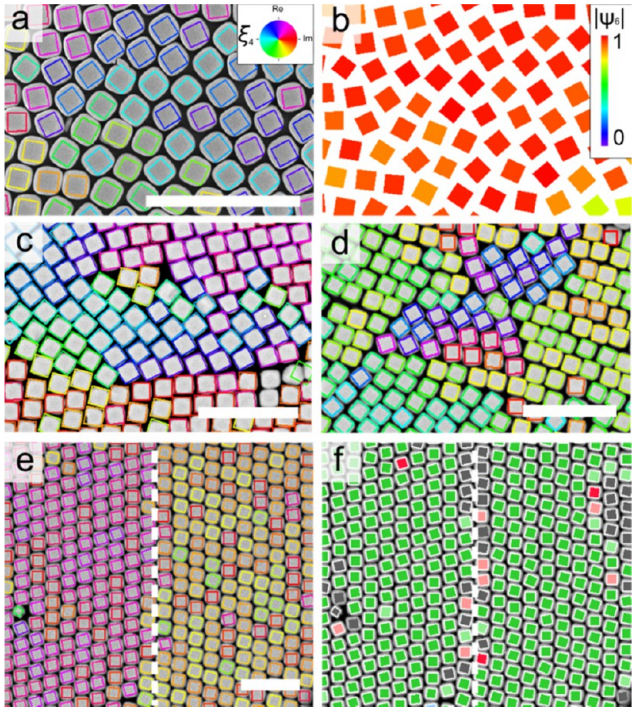

Figure 11. Different types of observed rotational disorder. (a) Dense packing of cubes with $m = 2.9$ in which the body orientation performs an almost full rotation from top to bottom. (b) Local 6-fold bond order parameter of the cubes in (a). (c, d) Orientationally disordered regions formed by cubes with $m = 3.5$. (e, f) Dense packing of cubes with $m = 3.6$ with the Λ_1-lattice displaying a twin boundary (white dashed line). Scale bars are 5 μm.

DOI: 10.1021/acs.langmuir.8b04330
Langmuir 2019, 35, 4946−4955

$$\Psi_6 = \frac{1}{N}\sum_{i\neq j}^{N} e^{6i\theta(r_{ij})} \quad (11)$$

where the sum runs over the total number N of NNs of particle i and $\theta(r_{ij})$ is defined as the angle between the vector connecting particles i and j and an arbitrary reference axis. Figure 11b shows that the orientational disorder does not disturb the positional order in the dense packing as the local $|\Psi_6| \sim 1$, indicating high 6-fold positional order. Of course, in this structure, almost no particles are identified with the Λ_0-lattice or Λ_1-lattice. This type of disorder might explain why the cubes with m = 2.9 have much less orientational order. Figure 11c,d shows, for cubes with m = 3.5, two typical examples of locally disordered regions of cubes with $|<\xi_4>| < 0.6$. Here, due to the alignment of cube faces, the body orientation changes gradually and is maintained over a few particle distances but is clearly misaligned with the larger structure. Besides rotational disorder, we also observed twinning of the Λ_1-lattices, characterized by a change in the local body orientation of the cubes. Figure 11e,f shows the body orientational change and the assignment of the Λ_1-lattice on both sides of the twin boundary.

CONCLUSIONS

We have investigated monolayers formed by convective assembly for three different hollow silica colloids that possess a cubic shape with different degrees of corner roundness. We find that with the CA method large densely packed monolayers of cubes with a high degree of order can be obtained. With SEM, the local orientational and positional orders in these monolayers were investigated in detail. We find that both predicted optimal packings, the Λ_0-lattice and Λ_1-lattice, as well as simple square-lattice packings and rotationally disordered packings, are formed. Using quantitative image analysis, we find that the Λ_0-lattice and the Λ_1-lattice easily transform into each other but that the Λ_1-lattice is more dominantly formed. In addition, an increase in m, i.e., a decrease in corner roundness, is found to lead to increased orientational order and an increase in the Λ_1-lattice formation, whereas the frequency of the Λ_0-lattice is unaffected by m. The formation of the different packings can be explained by the exact cube shape combined with the out-of-equilibrium convective assembly process. Strong immersion capillary forces, solvent flow, and pinned particles combined with the alignment of cube faces allow rows of particles to shift and induce the transformation between the optimal Λ_1-lattice and Λ_0-lattice. Moreover, these processes also seem responsible for the formation of packings with lower densities, including the simple square-lattice and orientationally disordered packings.

From our study, it is clear that even with the out-of-equilibrium CA process large ordered monolayers of cubes can be obtained whose orientational order as well as the occurrence of the Λ_1-lattice can be controlled by the shape parameter m. Further control over the monolayers could be obtained via one of the many optimization routes that have been established for spherical particles, such as meniscus pinning,[47] as well as template-directed assembly.[49] In future investigations, it would be interesting to see whether these methods can also be applied for controlling the order in the monolayers formed by the cubes. Especially, monolayers of cubes are of interest as functional materials, for example, as membranes in which the active component can be captured inside the hollow cube center.

AUTHOR INFORMATION

Corresponding Author

*E-mail: janne-mieke.meijer@uva.nl.

ORCID

Janne-Mieke Meijer: 0000-0002-5148-9948
Fabian Hagemans: 0000-0002-4748-8547
Andrei V. Petukhov: 0000-0001-9840-6014

Present Addresses

[‖]Institute of Physics, University of Amsterdam, Science Park 904, 1098 XH Amsterdam, The Netherlands (J.-M.M).
[⊥]Department of Explosions, Ballistics and Protection, TNO Defence, Security and Safety, Lange Kleiweg 137, 2280 AA Rijswijk, The Netherlands (V.M.).
[#]Institute of Physical Chemistry, RWTH Aachen University, Landoltweg 2, 52074 Aachen, Germany (F.H.).

Author Contributions

The manuscript was written through contributions of all authors. All authors have given approval to the final version of the manuscript.

Notes

The authors declare no competing financial interest.

ACKNOWLEDGMENTS

We thank Jan Hilhorst, Robert Löffler, Laura Rossi, and Jörg Roller for fruitful discussions. We also thank Hans Meeldijk and Chris Schneijdenberg for their assistance with the electron microscopes. J.-M.M. acknowledges financial support from the Alexander von Humboldt Foundation.

REFERENCES

(1) Vlasov, Y. A.; Bo, X.-Z.; Sturm, J. C.; Norris, D. J. On-chip natural assembly of silicon photonic bandgap crystals. *Nature* **2001**, *414*, 289−293.
(2) Marlow, F.; Muldarisnur; Sharifi, P.; Brinkmann, R.; Mendive, C. Opals: status and prospects. *Angew. Chem., Int. Ed.* **2009**, *48*, 6212−6233.
(3) Fenzl, C.; Hirsch, T.; Wolfbeis, O. S. Photonic crystals for chemical sensing and biosensing. *Angew. Chem., Int. Ed.* **2014**, *53*, 3318−3335.
(4) Xu, J.; Guo, Z. Biomimetic photonic materials with tunable structural colors. *J. Colloid Interface Sci.* **2013**, *406*, 1−17.
(5) Akerboom, S.; Pujari, S. P.; Turak, A.; Kamperman, M. Controlled Fabrication of Polypyrrole Surfaces with Overhang Structures by Colloidal Templating. *ACS Appl. Mater. Interfaces* **2015**, *7*, 16507−16517.
(6) Sciacca, B.; Berkhout, A.; Brenny, B. J. M.; Oener, S. Z.; van Huis, M. A.; Polman, A.; Garnett, E. C. Monocrystalline Nanopatterns Made by Nanocube Assembly and Epitaxy. *Adv. Mater.* **2017**, *29*, No. 1701064.
(7) Vogel, N.; Retsch, M.; Fustin, C. A.; Del Campo, A.; Jonas, U. Advances in colloidal assembly: the design of structure and hierarchy in two and three dimensions. *Chem. Rev.* **2015**, *115*, 6265−6311.
(8) Lotito, V.; Zambelli, T. Approaches to self-assembly of colloidal monolayers: A guide for nanotechnologists. *Adv. Colloid Interface Sci.* **2017**, *246*, 217−274.
(9) Jiang, P.; Bertone, J. F.; Hwang, K. S.; Colvin, V. L. Single-Crystal Colloidal Multilayers of Controlled Thickness. *Chem. Mater.* **1999**, *11*, 2132−2140.
(10) Prevo, B. G.; Kuncicky, D. M.; Velev, O. D. Engineered deposition of coatings from nano- and micro-particles: A brief review

DOI: 10.1021/acs.langmuir.8b04330
Langmuir 2019, 35, 4946−4955

of convective assembly at high volume fraction. *Colloids Surf., A* **2007**, *311*, 2−10.
(11) Denkov, N.; Velev, O.; Kralchevski, P.; Ivanov, I.; Yoshimura, H.; Nagayama, K. Mechanism of formation of two-dimensional crystals from latex particles on substrates. *Langmuir* **1992**, *8*, 3183−3190.
(12) Denkov, N. D.; Velev, O. D.; Kralchevsky, P. A.; Ivanov, I. B.; Yoshimura, H.; Nagayama, K. Two-dimensional crystallization. *Nature* **1993**, *361*, No. 26.
(13) Fleck, N. A.; McMeeking, R. M.; Kraus, T. Convective Assembly of a Particle Monolayer. *Langmuir* **2015**, *31*, 13655−13663.
(14) Deegan, R. D.; Bakajin, O.; Dupont, T. F.; Huber, G.; Nagel, S. R.; Witten, T. A. Capillary flow as the cause of ring stains from dried liquid drops. *Nature* **1997**, *389*, 827−829.
(15) Glotzer, S. C.; Solomon, M. J. Anisotropy of building blocks and their assembly into complex structures. *Nat. Mater.* **2007**, *6*, 557−562.
(16) Petukhov, A. V.; Meijer, J.-M.; Vroege, G. J. Particle shape effects in colloidal crystals and colloidal liquid crystals: Small-angle X-ray scattering studies with microradian resolution. *Curr. Opin. Colloid Interface Sci.* **2015**, *20*, 272−281.
(17) van Blaaderen, A. Colloids get complex. *Nature* **2006**, *439*, No. 545.
(18) Sacanna, S.; Pine, D. J. Shape-anisotropic colloids: Building blocks for complex assemblies. *Curr. Opin. Colloid Interface Sci.* **2011**, *16*, 96−105.
(19) Gong, Z.; Hueckel, T.; Yi, G. R.; Sacanna, S. Patchy particles made by colloidal fusion. *Nature* **2017**, *550*, 234−238.
(20) Manoharan, V. N. Colloidal matter: Packing, geometry, and entropy. *Science* **2015**, *349*, No. 1253751.
(21) Ravaine, S.; Duguet, E. Synthesis and assembly of patchy particles: Recent progress and future prospects. *Curr. Opin. Colloid Interface Sci.* **2017**, *30*, 45−53.
(22) Damasceno, P. F.; Engel, M.; Glotzer, S. C. Predictive self-assembly of polyhedra into complex structures. *Science* **2012**, *337*, 453−457.
(23) Porter, C. L.; Crocker, J. C. Directed assembly of particles using directional DNA interactions. *Curr. Opin. Colloid Interface Sci.* **2017**, *30*, 34−44.
(24) Dugyala, V. R.; Daware, S. V.; Basavaraj, M. G. Shape anisotropic colloids: synthesis, packing behavior, evaporation driven assembly, and their application in emulsion stabilization. *Soft Matter* **2013**, *9*, 6711−6725.
(25) Dugyala, V. R.; Basavaraj, M. G. Control over coffee-ring formation in evaporating liquid drops containing ellipsoids. *Langmuir* **2014**, *30*, 8680−8686.
(26) Riley, E. K.; Liddell, C. M. Confinement-controlled self assembly of colloids with simultaneous isotropic and anisotropic cross-section. *Langmuir* **2010**, *26*, 11648−11656.
(27) Rossi, L.; Sacanna, S.; Irvine, W. T. M.; Chaikin, P. M.; Pine, D. J.; Philipse, A. P. Cubic crystals from cubic colloids. *Soft Matter* **2011**, *7*, 4139−4142.
(28) Meijer, J.-M.; Hagemans, F.; Rossi, L.; Byelov, D. V.; Castillo, S. I.; Snigirev, A.; Snigireva, I.; Philipse, A. P.; Petukhov, A. V. Self-assembly of colloidal cubes via vertical deposition. *Langmuir* **2012**, *28*, 7631−7638.
(29) Castillo, S. I. R.; Ouhajji, S.; Fokker, S.; Erné, B. H.; Schneijdenberg, C. T. W. M.; Thies-Weesie, D. M. E.; Philipse, A. P. Silica cubes with tunable coating thickness and porosity: From hematite filled silica boxes to hollow silica bubbles. *Microporous Mesoporous Mater.* **2014**, *195*, 75−86.
(30) Rossi, L.; Soni, V.; Ashton, D. J.; Pine, D. J.; Philipse, A. P.; Chaikin, P. M.; Dijkstra, M.; Sacanna, S.; Irvine, W. T. Shape-sensitive crystallization in colloidal superball fluids. *Proc. Natl. Acad. Sci. U.S.A.* **2015**, *112*, 5286−5290.
(31) Meijer, J.-M.; Pal, A.; Ouhajji, S.; Lekkerkerker, H. N.; Philipse, A. P.; Petukhov, A. V. Observation of solid-solid transitions in 3D crystals of colloidal superballs. *Nat. Commun.* **2017**, *8*, No. 14352.
(32) Jiao, Y.; Stillinger, F. H.; Torquato, S. Optimal packings of superballs. *Phys. Rev. E* **2009**, *79*, No. 041309.
(33) Jiao, Y.; Stillinger, F. H.; Torquato, S. Optimal packings of superdisks and the role of symmetry. *Phys. Rev. Lett.* **2008**, *100*, No. 245504.
(34) Ni, R.; Gantapara, A. P.; de Graaf, J.; van Roij, R.; Dijkstra, M. Phase diagram of colloidal hard superballs: from cubes via spheres to octahedra. *Soft Matter* **2012**, *8*, 8826−8834.
(35) Sugimoto, T.; Sakata, K. Preparation of monodisperse pseudocubic α-Fe2O3 particles from condensed ferric hydroxide gel. *J. Colloid Interface Sci.* **1992**, *152*, 587−590.
(36) Graf, C.; Vossen, D. L. J.; Imhof, A.; van Blaaderen, A. A General Method To Coat Colloidal Particles with Silica. *Langmuir* **2003**, *19*, 6693−6700.
(37) Rossi, L.; Donaldson, J. G.; Meijer, J. M.; Petukhov, A. V.; Kleckner, D.; Kantorovich, S. S.; Irvine, W. T. M.; Philipse, A. P.; Sacanna, S. Self-organization in dipolar cube fluids constrained by competing anisotropies. *Soft Matter* **2018**, *14*, 1080−1087.
(38) Jiao, Y.; Stillinger, F. H.; Torquato, S. Distinctive features arising in maximally random jammed packings of superballs. *Phys. Rev. E* **2010**, *81*, No. 041304.
(39) Prevo, B. G.; Velev, O. D. Controlled, Rapid Deposition of Structured Coatings from Micro- and Nanoparticle Suspensions. *Langmuir* **2004**, *20*, 2099−2107.
(40) Avendaño, C.; Escobedo, F. A. Phase behavior of rounded hard-squares. *Soft Matter* **2012**, *8*, 4675−4681.
(41) Zhao, K.; Bruinsma, R.; Mason, T. G. Entropic crystal-crystal transitions of Brownian squares. *Proc. Natl. Acad. Sci. U.S.A.* **2011**, *108*, 2684−2847.
(42) Sanders, J. V. Close-packed structures of spheres of two different sizes I. Observations on natural opal. *Philos. Mag. A* **1980**, *42*, 705−720.
(43) Leunissen, M. E.; Christova, C. G.; Hynninen, A. P.; Royall, C. P.; Campbell, A. I.; Imhof, A.; Dijkstra, M.; van Roij, R.; van Blaaderen, A. Ionic colloidal crystals of oppositely charged particles. *Nature* **2005**, *437*, 235−240.
(44) Overgaag, K.; Evers, W.; de Nijs, B.; Koole, R.; Meeldijk, J.; Vanmaekelbergh, D. Binary Superlattices of PbSe and CdSe Nanocrystals. *J. Am. Chem. Soc.* **2008**, *130*, 7833−7835.
(45) Boles, M. A.; Engel, M.; Talapin, D. V. Self-Assembly of Colloidal Nanocrystals: From Intricate Structures to Functional Materials. *Chem. Rev.* **2016**, *116*, 11220−11289.
(46) Avci, C.; Imaz, I.; Carne-Sanchez, A.; Pariente, J. A.; Tasios, N.; Perez-Carvajal, J.; Alonso, M. I.; Blanco, A.; Dijkstra, M.; Lopez, C.; Maspoch, D. Self-assembly of polyhedral metal-organic framework particles into three-dimensional ordered superstructures. *Nat. Chem.* **2018**, *10*, 78−84.
(47) Ng, E. C.; Chin, K. M.; Wong, C. C. Controlling inplane orientation of a monolayer colloidal crystal by meniscus pinning. *Langmuir* **2011**, *27*, 2244−2249.
(48) Smallenburg, F.; Filion, L.; Marechal, M.; Dijkstra, M. Vacancy-stabilized crystalline order in hard cubes. *Proc. Natl. Acad. Sci. U.S.A.* **2012**, *109*, 17886−17890.
(49) Mishchenko, L.; Hatton, B.; Kolle, M.; Aizenberg, J. Patterning hierarchy in direct and inverse opal crystals. *Small* **2012**, *8*, 1904−1911.

DOI: 10.1021/acs.langmuir.8b04330
Langmuir 2019, 35, 4946−4955